Commun. Comput. Phys.
doi: 10.4208/cicp.091014.030515a

Vol. **21**, No. 2, pp. 443-465
February 2017

An Alternative Lattice Boltzmann Model for Incompressible Flows and its Stabilization

Liangqi Zhang[1,2], Zhong Zeng[1,3,*], Haiqiong Xie[1], Zhouhua Qiu[1], Liping Yao[4], Yongxiang Zhang[1] and Yiyu Lu[2]

[1] *Department of Engineering Mechanics, College of Aerospace Engineering, Chongqing University, Chongqing 400044, P.R. China.*
[2] *State Key Laboratory of Coal Mine Disaster Dynamics and Control, Chongqing University, Chongqing 400044, P.R. China.*
[3] *State Key laboratory of Crystal Material, Shandong University, Jinan 250100, P.R. China.*
[4] *College of Engineering and Technology, Southwest University, Chongqing 400716, P.R. China.*

Communicated by Kun Xu

Received 9 October 2014; Accepted (in revised version) 3 May 2015

Abstract. In this paper, an alternative lattice Boltzmann (LB) model for incompressible flows is proposed. By modifying directly the moments of the equilibrium distribution function (EDF), the continuous expression of the EDF in tensor Hermite polynomials is derived using the moment expansion and then discretized with the discrete velocity vectors of the D2Q9 lattice. The present model as well as its counterpart, the incompressible LB model proposed by Guo, reproduces the incompressible Navier-Stokes (N-S) equations for both steady and unsteady flows. Besides, an alternative pressure formula, which represents the pressure as the diagonal part of the stress tensor, is adopted in the present model. Furthermore, in order to enhance the stability of the present LB model, an additional relaxation time pertaining to the non-hydrodynamic mode is added to the BGK collision operator. The present LB model is validated by two benchmark tests: the cavity flow with different Reynolds number (Re) and the flow past an impulsively started cylinder at Re = 40 and 550.

PACS: 47.10.ab, 47.11.-j, 02.60.Cb

Key words: Lattice Boltzmann method, incompressible flows, cavity flow, deviatoric stress, compressibility effect.

*Corresponding author. *Email addresses:* liangqizhang@cqu.edu.cn, liangqizhang@ntu.edu.sg (L. Zhang), zzeng@cqu.edu.cn (Z. Zeng), xiehaiqiong@cqu.edu.cn (H. Xie), qiuzhouhua@cqu.edu.cn (Z. Qiu), lpyao@swu.edu.cn (L. Yao), zhangyx@cqu.edu.cn (Y. Zhang), luyiyu@cqu.edu.cn (Y. Lu)

 ©2017 Global-Science Press

https://doi.org/10.4208/cicp.091014.030515a Published online by Cambridge University Press

1 Introduction

The LB method, a promising alternative to conventional numerical methods for fluid dynamics, has win great popularity owing to its successful application in complex fluids such as suspensions and interfacial dynamics [1–6]. The LB method is essentially a second-order explicit finite difference approximation of the relevant macroscopic equations [7, 8]. The superior features of LB method over its second order finite difference counterparts based on direct discretization of the Navier-Stokes (N-S) equations are its low numerical dissipation and better isotropy [1, 9, 10].

The LB method consists of two core components: the lattice Boltzmann equation (LBE), governing the evolution of the distribution function, and the relationships, represented by the moment equations of the distribution function, between the distribution function and the macroscopic variables. By applying the Chapman-Enskog expansion [11–13], the macroscopic N-S equations can be derived from the LBE, and the specific forms of the relevant macroscopic equations largely depend on the moments of the equilibrium distribution function (EDF). With the prescribed EDF of the standard LB model, the isothermal, compressible N-S equations are obtained, and the solutions of incompressible equations are approximated by this model with second order error in Mach number (Ma) [9]. In order to reduce the compressibility error in the standard LB model, an incompressible LB model, notated as He-Luo model, is proposed by He and Luo [14,15], in which the fluid density ρ is replaced by a constant mean density ρ_0 everywhere ρ is multiplied by the fluid velocity $\mathbf{u}$. The macroscopic equations derived from this model approximate the incompressible N-S equation with $\mathcal{O}(Ma^3)$ error for steady flow. However, for unsteady flow, the compressibility error associated with the continuity equation remains $\mathcal{O}(Ma^2)$ [9,14]. Based on the assumptions that the fluid density is a uniform constant and the fluid pressure is independent of density, another incompressible LB model was designed by Guo in 2000 [16]. And the resulting macroscopic equations pertaining to Guo's model are incompressible for both steady and unsteady flows. Although the error of the corresponding momentum equation is of the order $\mathcal{O}(Ma^2)$, the compressibility error is eliminated by setting the fluid density to be a constant.

In this work, inspired from Guo's model, an alternative incompressible LB model is proposed by using Grad's moment expansion [17, 18]. The present model inherits the advantageous features of Guo's model, i.e. the compressibility error associated with the continuity equation vanishes. Besides, an alternative pressure formula, which accords with the definition of the mechanical pressure [12], is adopted in the present model and provides more accurate evaluation of the deviatoric stress than Guo's model. Moreover, the equivalent moment systems in the diffusive scale, derived by M. Junk [7, 8], demonstrate that the truncated error term, $\Delta\rho$, linked to the Laplacian of pressure for the standard LB model and the He-Luo model, has explicit effect on the mass conservation and the accuracy of the modeled stress tensor [19]. Theoretically, with the basic assumption that the fluid density is a uniform constant, the present model and the Guo's model are expected to reduce such error.

https://doi.org/10.4208/cicp.091014.030515a Published online by Cambridge University Press

Based on the stability analysis in [9,13,20], the coupling between hydrodynamic and non-hydrodynamic modes [21, 22] may lead to the instability of the LB algorithms. In this work, inspired from the multiple relaxation time (MRT) collision operator [9, 10, 15, 23–25] and the Regularized Lattice BGK (RLBGK) scheme [26–28], in which the non-hydrodynamic modes (i.e. the ghost modes) are suppressed to stabilize the LB model, an extra relaxation time $\tau_{\mathbf{J}}$ in the BGK operator [29] is introduced to damp the relevant ghost mode **J**, a primary ghost mode coupling with the hydrodynamic modes, therefore, the stability of the present model is highly enhanced.

The present model is validated for both steady and unsteady benchmark tests. Comparing with the other three LB models, the present model provides better accuracy near the solid walls for the cavity flow, and pressure drag history obtained from both the present model and Guo's model is more in line with the elliptic incompressibility condition in simulating flow past an impulsively started cylinder.

2 Lattice Boltzmann hydrodynamics

2.1 The standard LB model

In the LB method, the macroscopic variables such as the fluid density ρ and velocity $\mathbf{u}$ are defined by the moments of the discrete distribution function f_α as

$$\sum_\alpha f_\alpha = \rho, \tag{2.1}$$

$$\sum_\alpha f_\alpha \xi_{\alpha i} = \rho u_i, \tag{2.2}$$

$$\sum_\alpha f_\alpha \xi_{\alpha i}\xi_{\alpha j} = \Pi_{ij}, \tag{2.3}$$

where the second order tensor $\Pi_{ij}=\rho u_i u_j + P_{ij}$ is the momentum flux, and $P_{ij}=p\delta_{ij}-\tau_{ij}$ is the stress tensor with τ_{ij} being the deviatoric stress.

The lattice Boltzmann BGK equation is introduced as

$$f_\alpha(\mathbf{x}+\boldsymbol{\xi}_\alpha dt, t+dt) - f_\alpha(\mathbf{x},t) = -\frac{1}{\tau}[f_\alpha(\mathbf{x},t) - f_\alpha^{(0)}(\mathbf{x},t)], \tag{2.4}$$

where τ is the single relaxation time of the BGK collision operator [29]; f_α and $f_\alpha^{(0)}$ are the discrete form of distribution function and its equilibrium version, respectively. The discrete velocity vectors $\boldsymbol{\xi}_\alpha$ in Eq. (2.4) are defined as below

$$\boldsymbol{\xi}_\alpha = \begin{cases} (0,0), & \alpha=0, \\ c(\cos[(\alpha-1)\pi/2], \sin[(\alpha-1)\pi/2]), & \alpha=1,2,3,4, \\ \sqrt{2}c(\cos[(2\alpha-1)\pi/4], \sin[(2\alpha-1)\pi/4]), & \alpha=5,6,7,8, \end{cases} \tag{2.5}$$

where $c=dx/dt$, and dx, dt are the spatial and time step, respectively. Moreover, in the following simulations, dx and dt are both set as the dimensionless constant 1.

https://doi.org/10.4208/cicp.091014.030515a Published online by Cambridge University Press

As for the standard LB model [30], the EDF is given by

$$f_\alpha^{(0)}=\rho w_\alpha\left\{1+\frac{\boldsymbol{\xi}_\alpha\bullet\mathbf{u}}{RT}+\frac{(\boldsymbol{\xi}_\alpha\bullet\mathbf{u})^2}{2(RT)^2}-\frac{\mathbf{u}^2}{2RT}\right\} \tag{2.6}$$

in units where $RT=c_s^2=1/3$, and the components of the discrete velocity vectors take the integer value $\{-1,0,1\}$. $w_0=4/9$, $w_{1,2,3,4}=1/9$, $w_{5,6,7,8}=1/36$ are weight coefficients of the D2Q9 lattice. The moments of the EDF in Eq. (2.6) are

$$\sum_\alpha f_\alpha^{(0)}=\rho, \tag{2.7}$$

$$\sum_\alpha f_\alpha^{(0)}\xi_{\alpha i}=\rho u_i, \tag{2.8}$$

$$\sum_\alpha f_\alpha^{(0)}\xi_{\alpha i}\xi_{\alpha j}=\rho u_i u_j+p\delta_{ij}. \tag{2.9}$$

With above moments, the isothermal, compressible N-S equations are obtained as

$$\frac{1}{RT}\frac{\partial}{\partial t}p+\nabla\bullet(\rho\mathbf{u})=0, \tag{2.10}$$

$$\frac{\partial}{\partial t}(\rho\mathbf{u})+\nabla\bullet(\rho\mathbf{u}\mathbf{u}+pI-\boldsymbol{\tau})=0, \tag{2.11}$$

$$\tau_{ij}=\rho RT\left(\tau-\frac{1}{2}\right)dt\left(\frac{\partial u_i}{\partial x_j}+\frac{\partial u_j}{\partial x_i}\right)+\mathcal{O}(Ma^3), \tag{2.12}$$

where $p=\rho RT$ is the fluid pressure. In the low Ma limit, the solutions of above macroscopic equations approximate the incompressible N-S equations with error $\mathcal{O}(Ma^2)$.

2.2 Incompressible LB models

In the He-Luo model [14, 15], the fluid density ρ is decomposed of two parts: the mean density ρ_0 and the density fluctuation $\delta\rho$ which is of the order $\mathcal{O}(Ma^2)$. Substituting $\rho=\rho_0+\delta\rho$ into the EDF of the standard model in Eq. (2.6), and neglecting the terms of the order $\mathcal{O}(Ma^3)$, the EDF $f_\alpha^{(0)}$ of the He-Luo model is expressed as

$$f_\alpha^{(0)}=\rho w_\alpha+\rho_0 w_\alpha\left[\frac{\boldsymbol{\xi}_\alpha\bullet\mathbf{u}}{RT}+\frac{(\boldsymbol{\xi}_\alpha\bullet\mathbf{u})^2}{2(RT)^2}-\frac{\mathbf{u}^2}{2RT}\right] \tag{2.13}$$

and the corresponding moments are

$$\sum_\alpha f_\alpha^{(0)}=\rho, \tag{2.14}$$

$$\sum_\alpha f_\alpha^{(0)}\xi_{\alpha i}=\rho_0 u_i, \tag{2.15}$$

$$\sum_\alpha f_\alpha^{(0)}\xi_{\alpha i}\xi_{\alpha j}=\rho_0 u_i u_j+p\delta_{ij}, \tag{2.16}$$

https://doi.org/10.4208/cicp.091014.030515a Published online by Cambridge University Press

which reproduce the Chorin's artificial compressibility equations

$$\frac{1}{RT}\frac{\partial}{\partial t}p+\nabla\bullet\mathbf{u}=0, \tag{2.17}$$

$$\frac{\partial}{\partial t}\mathbf{u}+\nabla\bullet(\mathbf{uu}+pI-\boldsymbol{\tau})=0, \tag{2.18}$$

$$\tau_{ij}=RT(\tau-\frac{1}{2})dt\left(\frac{\partial u_i}{\partial x_j}+\frac{\partial u_j}{\partial x_i}\right)+\mathcal{O}(Ma^3), \tag{2.19}$$

where $p=\rho RT/\rho_0$ is the pressure. Above macroscopic equations approximate the incompressible N-S equations with $\mathcal{O}(Ma^3)$ error for steady flow, which is one order in Ma higher than the standard model. However, the compressibility error associated with the continuity equation remains $\mathcal{O}(Ma^2)$ [9].

To eliminate the compressibility error, by setting the fluid density to be a uniform constant, another incompressible LB model is built by Guo, EDF $f_\alpha^{(0)}$ of which is given as

$$f_\alpha^{(0)}=\begin{cases}\rho_0-(1-w_0)\dfrac{p}{RT}+\rho_0^* s_0(\mathbf{u}), & \alpha=0,\\ w_\alpha\dfrac{p}{RT}+\rho_0^* s_\alpha(\mathbf{u}), & \alpha=1-8,\end{cases} \tag{2.20}$$

$$s_\alpha(\mathbf{u})=w_\alpha\left[\frac{\boldsymbol{\xi}_\alpha\bullet\mathbf{u}}{RT}+\frac{(\boldsymbol{\xi}_\alpha\bullet\mathbf{u})^2}{2(RT)^2}-\frac{\mathbf{u}^2}{2RT}\right],$$

where $\rho_0=0$ is constant density in the zero-order moment of the EDF, and $\rho_0^*=1$ is the density relating to the first and higher moments of the distribution function

$$\sum_\alpha f_\alpha^{(0)}=0, \tag{2.21}$$

$$\sum_\alpha f_\alpha^{(0)}\xi_{\alpha i}=u_i, \tag{2.22}$$

$$\sum_\alpha f_\alpha^{(0)}\xi_{\alpha i}\xi_{\alpha j}=u_iu_j+p\delta_{ij}. \tag{2.23}$$

The moment equations given by Eqs. (2.21)-(2.23) yields the incompressible N-S equations

$$\nabla\bullet\mathbf{u}=0, \tag{2.24}$$

$$\frac{\partial}{\partial t}\mathbf{u}+\nabla\bullet(\mathbf{uu}+pI-\boldsymbol{\tau})=0, \tag{2.25}$$

$$\tau_{ij}=RT(\tau-\frac{1}{2})dt\left(\frac{\partial u_i}{\partial x_j}+\frac{\partial u_j}{\partial x_i}\right)+\mathcal{O}(Ma^2). \tag{2.26}$$

Although the resulting momentum equation accords the incompressible one with $\mathcal{O}(Ma^2)$ error, the compressibility error term, $\frac{1}{RT}\frac{\partial p}{\partial t}$, is eliminated by the constant fluid density.

https://doi.org/10.4208/cicp.091014.030515a Published online by Cambridge University Press

The fluid pressure and velocity, the independent macroscopic variables in Guo's model, are determined as

$$\mathbf{u}=\sum_{\alpha} f_{\alpha}\boldsymbol{\xi}_{\alpha}, \tag{2.27}$$

$$p=\frac{RT}{(1-w_0)}\left[\sum_{\alpha=1}^{8} f_{\alpha}+s_0(\mathbf{u})\right]. \tag{2.28}$$

In the pressure computation (i.e. Eq. (2.28)), an approximation is introduced as

$$\sum_{\alpha=1}^{8} f_{\alpha}=-f_0\approx -f_0^{(0)}. \tag{2.29}$$

According to Grad's 13 moment system [17,18], there is

$$f=f^{(0)}\left[1-\frac{\tau_{ij}}{2pRT}(\xi-u)_i(\xi-u)_j\right]. \tag{2.30}$$

Obviously, the truncation errors of the approximation given by Eq. (2.29) are proportional to τ_{ij} times Ma squared from the u_iu_j/RT factor.

3 An alternative LB model for incompressible and homogeneous flows

3.1 The derivation of the present model

From thorough analysis of the above LB models, we conclude that the moments of EDF should be revised to the form of Guo's model for the purpose to obtain the standard incompressible N-S equations. Therefore, the moments of the distribution function is firstly determined as

$$\int f^{(0)}d\boldsymbol{\xi}=\rho_0, \tag{3.1}$$

$$\int f^{(0)}\xi_i d\boldsymbol{\xi}=\rho_0 u_i, \tag{3.2}$$

$$\int f^{(0)}\xi_i\xi_j d\boldsymbol{\xi}=\rho_0 u_iu_j+p\delta_{ij}, \tag{3.3}$$

$$\int f d\boldsymbol{\xi}=\rho_0, \tag{3.4}$$

$$\int f\xi_i d\boldsymbol{\xi}=\rho_0 u_i, \tag{3.5}$$

$$\int f\xi_i\xi_j d\boldsymbol{\xi}=\rho_0 u_iu_j+P_{ij}, \tag{3.6}$$

https://doi.org/10.4208/cicp.091014.030515a Published online by Cambridge University Press

where ρ_0 is the constant density, and p, the pressure, is independent of density. With the assistance of Grad's Hermite tensorial polynomials [17, 18], the continuous form of the EDF in the present model is derived from the moments of the EDF given by Eqs. (3.1), (3.2) and (3.3)

$$f^{(0)}=\frac{\rho_0}{(2\pi RT)^{D/2}}\exp\Big(-\frac{\boldsymbol{\xi}^2}{2RT}\Big)\Big\{1+\frac{\boldsymbol{\xi}\bullet\mathbf{u}}{RT}+\frac{(\boldsymbol{\xi}\bullet\mathbf{u})^2}{2(RT)^2}-\frac{\mathbf{u}^2}{2RT}+\Big(\frac{p}{\rho_0 RT}-1\Big)\Big(\frac{\boldsymbol{\xi}^2}{2RT}-\frac{D}{2}\Big)\Big\}, \tag{3.7}$$

where D is the spatial dimensions.

To evaluate numerically the hydrodynamic moments in Eqs. (3.1)-(3.6), the phase space $\boldsymbol{\xi}$ is discretized [31] as

$$\int f(x,\boldsymbol{\xi},t)\psi(\boldsymbol{\xi})d\boldsymbol{\xi}=\sum_\alpha W_\alpha\psi(\boldsymbol{\xi}_\alpha)f(x,\boldsymbol{\xi}_\alpha,t), \tag{3.8}$$

where $\psi(\boldsymbol{\xi})$ is a polynomial of $\boldsymbol{\xi}$, W_α is the weight coefficient of the quadrature, and $\boldsymbol{\xi}_\alpha$ is the discrete velocity set. Accordingly, the continuous moments can be computed by

$$\rho_0=\sum_\alpha f_\alpha=\sum_\alpha f_\alpha^{(0)}, \tag{3.9}$$

$$\rho_0 u_i=\sum_\alpha f_\alpha\xi_{\alpha i}=\sum_\alpha f_\alpha^{(0)}\xi_{\alpha i}, \tag{3.10}$$

$$\rho_0 u_i u_j+p\delta_{ij}=\sum_\alpha f_\alpha^{(0)}\xi_{\alpha i}\xi_{\alpha j}, \tag{3.11}$$

$$\rho_0 u_i u_j+P_{ij}=\sum_\alpha f_\alpha\xi_{\alpha i}\xi_{\alpha j}, \tag{3.12}$$

where

$$f_\alpha=W_\alpha f(x,\boldsymbol{\xi}_\alpha,t), \tag{3.13}$$

$$f_\alpha^{(0)}=W_\alpha f^{(0)}(x,\boldsymbol{\xi}_\alpha,t). \tag{3.14}$$

By applying the D2Q9 lattice model, the continuous EDF in Eq. (3.7) is discretized as

$$f_\alpha^{(0)}=\rho_0 w_\alpha\left\{1+\frac{\mathbf{u}\bullet\boldsymbol{\xi}_\alpha}{RT}+\frac{(\mathbf{u}\bullet\boldsymbol{\xi}_\alpha)^2}{2(RT)^2}-\frac{\mathbf{u}^2}{2RT}+\Big(\frac{p}{\rho_0 RT}-1\Big)\Big(\frac{\boldsymbol{\xi}_\alpha^2}{2RT}-1\Big)\right\} \tag{3.15}$$

with $W_\alpha=(2\pi RT)^{D/2}\exp(\frac{\boldsymbol{\xi}_\alpha^2}{2RT})w_\alpha$. In particular, we set $\rho_0=1$, and discrete EDF in Eq. (3.15) is rewritten as

$$f_\alpha^{(0)}=\begin{cases}\dfrac{8}{9}-\dfrac{4p}{9RT}+s_0(\mathbf{u}), & \alpha=0,\\ \dfrac{1}{18}+\dfrac{p}{18RT}+s_\alpha(\mathbf{u}), & \alpha=1,2,3,4,\\ -\dfrac{1}{36}+\dfrac{p}{18RT}+s_\alpha(\mathbf{u}), & \alpha=5,6,7,8.\end{cases} \tag{3.16}$$

https://doi.org/10.4208/cicp.091014.030515a Published online by Cambridge University Press

In addition, the present model is completed by the following calculation of the macroscopic variables

$$\mathbf{u}=\sum_{\alpha} f_{\alpha}\boldsymbol{\xi}_{\alpha}, \tag{3.17}$$

$$p=\left(\sum_{\alpha} f_{\alpha}\xi_{\alpha i}\xi_{\alpha i}-u_i u_i\right)/2. \tag{3.18}$$

The pressure formula for the present model accords exactly with the definition of the mechanical pressure which represents the pressure as one-third the trace of the stress tensor [12]. In particular, the stress tensor is derived from the second-order moment of the distribution function as

$$P_{ij}=p\delta_{ij}-\tau_{ij}=\Pi_{ij}-\rho u_i u_j=\sum_{\alpha} f_{\alpha}\xi_{\alpha i}\xi_{\alpha j}-\rho u_i u_j,$$

which leads to the pressure formula under the incompressible limit $\tau_{ii}=0$

$$p=\frac{1}{D}\left(\sum_{\alpha} f_{\alpha}\boldsymbol{\xi}_{\alpha}^2-\rho\mathbf{u}^2\right).$$

It is noted that, in the conventional kinetic theory, the first term on the right hand of the pressure formula is related to total energy E as

$$\rho E=\rho\left(\varepsilon+\frac{\mathbf{u}^2}{2}\right)=\sum_{\alpha} f_{\alpha}\boldsymbol{\xi}_{\alpha}^2/2,$$

which is applied to determine the temperature T according to the definition of the internal energy $\varepsilon=DRT/2$ and the state equation for ideal gas $p=\rho RT$

$$T=\frac{1}{\rho DR}\left(\sum_{\alpha} f_{\alpha}\boldsymbol{\xi}_{\alpha}^2-\rho\mathbf{u}^2\right).$$

However, in accordance with the incompressibility condition, the ideal gas state equation is replaced by the assumption that the fluid pressure is independent of the density and fluid density in the present model is a constant. Therefore, the temperature expression is no longer available for the present model. Besides, the present model is proposed under the framework of incompressible and isothermal flows, and thus the temperature is of no physical significance here. Moreover, the present model is theoretically expected to be more accurate in the region of high shear stress since the approximation of Eq. (2.29) is avoided with the present pressure formula.

Undoubtedly, since the moments in Eqs. (3.9), (3.10) and (3.11) are similar with those of Guo's model, the N-S equations for incompressible flow are recovered from the present model with the same accuracy in Ma.

https://doi.org/10.4208/cicp.091014.030515a Published online by Cambridge University Press

3.2 The non-hydrodynamic modes and the stabilization in the present model

The EDF of the present model is constructed by the first three tensor Hermite polynomials 1, $\boldsymbol{\xi}_\alpha$ and $(\boldsymbol{\xi}_\alpha\boldsymbol{\xi}_\alpha-\frac{1}{3}I)$, the components of which comprise the six polynomials 1, $\xi_{\alpha x}$, $\xi_{\alpha y}$, $\xi_{\alpha x}^2-\frac{1}{3}$, $\xi_{\alpha x}\xi_{\alpha y}$ and $\xi_{\alpha y}^2-\frac{1}{3}$. Each of these polynomials may be regarded as a nine-dimensional lattice vector

$$|1\rangle=(1,1,1,1,1,1,1,1,1)^T, \tag{3.19a}$$
$$|\xi_{\alpha x}\rangle=(0,1,0,-1,0,1,-1,-1,1)^T, \tag{3.19b}$$
$$|\xi_{\alpha y}\rangle=(0,0,1,0,-1,1,1,-1,-1)^T, \tag{3.19c}$$
$$\left|\xi_{\alpha x}^2-\frac{1}{3}\right\rangle=\frac{1}{3}(-1,2,-1,2,-1,2,2,2,2)^T, \tag{3.19d}$$
$$|\xi_{\alpha x}\xi_{\alpha y}\rangle=(0,0,0,0,0,1,-1,1,-1)^T, \tag{3.19e}$$
$$\left|\xi_{\alpha y}^2-\frac{1}{3}\right\rangle=\frac{1}{3}(-1,-1,2,-1,2,2,2,2,2)^T. \tag{3.19f}$$

These polynomials are orthogonal with respect to the weighted inner product $\langle p,q\rangle=\sum_\alpha w_\alpha p_\alpha q_\alpha$, which is the direct analogy of the orthogonality of the continuous tensor Hermite polynomials [17,18].

The above six orthogonal lattice vectors in Eq. (3.19) may be completed to form an R^9 orthogonal basis with the "ghost vectors" g_α and $g_\alpha\boldsymbol{\xi}_\alpha$ [13,20–22]

$$|g_\alpha\rangle=\frac{9}{2}\left(|\boldsymbol{\xi}_\alpha|^4-\frac{15}{9}|\boldsymbol{\xi}_\alpha|^2+\frac{2}{9}\right)=(1,-2,-2,-2,-2,4,4,4,4)^T, \tag{3.20a}$$
$$|g_\alpha\xi_{\alpha x}\rangle=(0,-2,0,2,0,4,-4,-4,4)^T, \tag{3.20b}$$
$$|g_\alpha\xi_{\alpha y}\rangle=(0,0,-2,0,2,4,4,-4,-4)^T. \tag{3.20c}$$

The non-hydrodynamic (ghost) variables pertaining to the "ghost vectors" are defined as

$$N=\sum_\alpha f_\alpha g_\alpha, \tag{3.21}$$
$$\mathbf{J}=\sum_\alpha f_\alpha g_\alpha\boldsymbol{\xi}_\alpha. \tag{3.22}$$

Taking the moments of the discrete Boltzmann equation

$$\frac{\partial f_\alpha}{\partial t}+\xi_{\alpha k}\frac{\partial f_\alpha}{\partial x_k}=-\frac{1}{\tau_f}(f_\alpha-f_\alpha^{(eq)}), \tag{3.23}$$

https://doi.org/10.4208/cicp.091014.030515a Published online by Cambridge University Press

the hydrodynamic equations together with the ghost component equations are obtained

$$\nabla \bullet \mathbf{u} = 0, \tag{3.24a}$$

$$\frac{\partial}{\partial t}\mathbf{u} + \nabla \bullet \mathbf{\Pi} = 0, \tag{3.24b}$$

$$\frac{\partial}{\partial t}\mathbf{\Pi} + \nabla \bullet \left(\sum_{\alpha} f_\alpha \boldsymbol{\xi}_\alpha \boldsymbol{\xi}_\alpha \boldsymbol{\xi}_\alpha\right) = -\frac{1}{\tau_f}(\mathbf{\Pi} - \mathbf{\Pi}^{(0)}), \tag{3.24c}$$

$$\frac{\partial}{\partial t}N + \nabla \bullet \mathbf{J} = -\frac{1}{\tau_f}(N - N^{(0)}), \tag{3.24d}$$

$$\frac{\partial}{\partial t}\mathbf{J} + \nabla \bullet \left(\sum_{\alpha} f_\alpha g_\alpha \boldsymbol{\xi}_\alpha \boldsymbol{\xi}_\alpha\right) = -\frac{1}{\tau_f}(\mathbf{J} - \mathbf{J}^{(0)}). \tag{3.24e}$$

Considering that the components of the discrete velocity $\boldsymbol{\xi}_\alpha$ are integer values $\{-1,0,1\}$, the components of $\boldsymbol{\xi}_\alpha\boldsymbol{\xi}_\alpha\boldsymbol{\xi}_\alpha$ and $g_\alpha\boldsymbol{\xi}_\alpha\boldsymbol{\xi}_\alpha$ may be rewritten as

$$g_\alpha \xi_{\alpha x}\xi_{\alpha x} = 2\left(\xi_{\alpha y}\xi_{\alpha y} - \frac{1}{3}\right) + \frac{2}{3}g_\alpha, \tag{3.25a}$$

$$g_\alpha \xi_{\alpha x}\xi_{\alpha y} = 4\xi_{\alpha x}\xi_{\alpha y}, \tag{3.25b}$$

$$\xi_{\alpha x}\xi_{\alpha x}\xi_{\alpha y} = \frac{1}{3}\xi_{\alpha y} + \frac{1}{6}g_\alpha \xi_{\alpha y}. \tag{3.25c}$$

The relationships in Eq. (3.25) induce the cross coupling between the hydrodynamic and non-hydrodynamic modes, as demonstrated in Eqs. (3.24c), (3.24d) and (3.24e). As suggested in the Chapman-Enskog analysis, the non-hydrodynamic modes have no direct effect on the hydrodynamic equations. However, the coupling between the hydrodynamic and ghost modes leads to instability of the LB algorithms (refer to Dellar's work [9,13,20] for detailed stability analysis of the LB schemes).

With the orthogonal basis defined by Eqs. (3.19) and (3.20), the MRT collision operator is essentially expressed as

$$\begin{aligned}\Omega_\alpha = -w_\alpha \Bigg[&\frac{9}{2}s_3 M_{xx}^{(neq)} Q_{\alpha xx} + 9s_4 M_{xy}^{(neq)} Q_{\alpha xy} + \frac{9}{2}s_5 M_{yy}^{(neq)} Q_{\alpha yy} \\ &+ g_\alpha\left(\frac{1}{4}s_6 N + \frac{3}{8}s_7 J_x \xi_{\alpha x} + \frac{3}{8}s_8 J_y \xi_{\alpha y}\right)\Bigg],\end{aligned} \tag{3.26}$$

where $\mathbf{Q}_\alpha = (\boldsymbol{\xi}_\alpha\boldsymbol{\xi}_\alpha - \frac{1}{3}\mathbf{I})$; s_i are the adjustable relaxation parameters; $\mathbf{M}^{(neq)}$ is the non-equilibrium part of the second-order hydrodynamic mode

$$\mathbf{M}^{(neq)} = \sum_{\alpha}(f_\alpha - f_\alpha^{(0)})(\boldsymbol{\xi}_\alpha\boldsymbol{\xi}_\alpha - \frac{1}{3}\mathbf{I}). \tag{3.27}$$

Moreover, discarding the ghost contributions in the non-equilibrium part of the post-collision distribution function, the RLBGK scheme [26–28] is proposed to improve the

https://doi.org/10.4208/cicp.091014.030515a Published online by Cambridge University Press

stability of the BGK LB model

$$f_\alpha(\mathbf{x}+\boldsymbol{\xi}_\alpha dt,t+dt)=f_\alpha^{(0)}(\mathbf{x},t)+\frac{9(1-\omega)w_\alpha}{2}\mathbf{Q}_\alpha:\mathbf{M}^{(neq)}, \tag{3.28}$$

where $\omega=1/\tau$.

In this work, in order to enhance the stability of the present model, an additional relaxation time $\tau_{\mathbf{J}}$ is introduced to suppress the non-hydrodynamic mode **J**. The revised LBE is given by

$$f_\alpha(\mathbf{x}+\boldsymbol{\xi}_\alpha dt,t+dt)-f_\alpha(\mathbf{x},t)=-\frac{1}{\tau}[f_\alpha(\mathbf{x},t)-f_\alpha^{(0)}(\mathbf{x},t)]-\left(\frac{1}{\tau_{\mathbf{J}}}-\frac{1}{\tau}\right)\frac{3}{8}w_\alpha g_\alpha\boldsymbol{\xi}_\alpha\bullet\mathbf{J}. \tag{3.29}$$

When choosing $\tau_{\mathbf{J}}=1$, the non-hydrodynamic variable **J** would be damped maximally. Since **J** is the primary ghost mode coupling with the hydrodynamic modes, the stability of the present model is, therefore, highly enhanced with the treatment in Eq. (3.29).

4 Numerical results

In this section, in order to assess the present incompressible LB model, we present the results of two benchmark tests: the cavity flow with different Re, and the flow past an impulsively started cylinder at Re= 40 and 550.

4.1 The steady cavity flow

4.1.1 The velocity profiles

As a representative benchmark test, the cavity flow has been widely adopted to evaluate numerical methods [15, 16, 32, 33]. The general flow structures such as the locations and strengths of the vortexes are also successfully obtained from the LB simulations [15,16,31]. In this work, more attention is devoted to the velocity profiles to compare the numerical performances of the concerned LB models.

The simulations are organized as follows: the uniform driving velocity of the top wall $U=c_sMa$, where the sound speed $c_s=1/\sqrt{3}$; the characteristic length of the square cavity L equals the number of space steps N_x-1 (N_x is the number of grid points on the x direction) since the space step dx is dimensionless constant 1; the Reynolds number is determined as $\mathrm{Re}=UL/\nu$ and the cases of Re= 100, 400 and 1000 are included; all cases are simulated on the 129×129 lattice. With the prescribed Re, which is the only dimensionless controlling parameter in the cavity flow, the results from the LB models are comparable to the reference results [32]. And the relating relaxation time τ can be determined from the definition of the kinematic viscosity coefficient

$$\nu=\frac{(2\tau-1)}{6}. \tag{4.1}$$

https://doi.org/10.4208/cicp.091014.030515a Published online by Cambridge University Press

Therefore, with the prescribed Ma, $Ma=0.173$, 0.173, 0.115 for Re$=$100, 400 and 1000, respectively, the relevant relaxation time is determined.

In addition, the non-equilibrium extrapolation scheme [34] is adopted to implement the non-slip boundary uniformly for the four LB models. Lastly, the convergence criterion as below is applied

$$\frac{\sum_{i,j}\sqrt{(u_0(i,j)-u_1(i,j))^2+(v_0(i,j)-v_1(i,j))^2}}{\sum_{i,j}\sqrt{u_0^2(i,j)+v_0^2(i,j)}}<5.0\times10^{-7}, \tag{4.2}$$

where $u_0(i,j)$, $v_0(i,j)$ are the x and y velocity components at time t, respectively; $u_1(i,j)$, $v_1(i,j)$ are the velocity components at $t+dt$.

Fig. 1 gives the profiles of the velocity components along the horizontal and vertical centerlines for Re$=$400 and 1000. For Re$=$100, all the solutions of four LB models agree well with those of the FDM [32]. When the Re increases to 400 and 1000, the visible deviations between the velocity components given by other three LB models (the standard

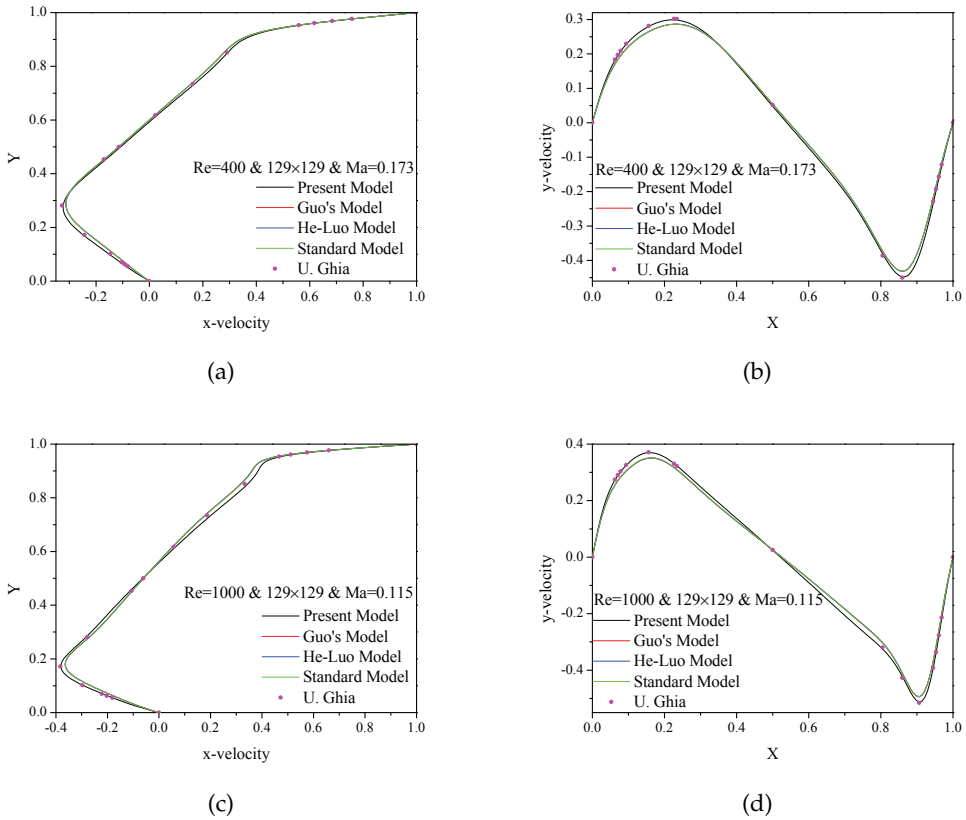


Figure 1: The velocity components, u (left) and v (right), along the vertical and horizontal centerlines for Re$=$400 (a and b), and 1000 (c and d), the reference results from the literature [32] are notated as 'U. Ghia'.

https://doi.org/10.4208/cicp.091014.030515a Published online by Cambridge University Press

Table 1: The comparisons of x-velocity on the vertical centerline for Re=400 and 1000.

	Re=400					Re=1000				
Y	U. Ghia	Present Model	Guo's Model	He-Luo Model	Standard Model	U. Ghia	Present Model	Guo's Model	He-Luo Model	Standard Model
0.0547	-0.0819	-0.0865	-0.0738	-0.0740	-0.0734	-0.1811	-0.1791	-0.1579	-0.1583	-0.1582
0.0625	-0.0927	-0.0977	-0.0836	-0.0839	-0.0832	-0.2020	-0.1997	-0.1770	-0.1774	-0.1773
0.0703	-0.1034	-0.1087	-0.0934	-0.0937	-0.0930	-0.2222	-0.2199	-0.1957	-0.1961	-0.1961
0.1016	-0.1461	-0.1523	-0.1328	-0.1331	-0.1322	-0.2973	-0.2949	-0.2675	-0.2681	-0.2682
0.1719	-0.2430	-0.2479	-0.2239	-0.2243	-0.2233	-0.3829	-0.3807	-0.3626	-0.3631	-0.3638
0.2813	-0.3273	-0.3224	-0.3122	-0.3123	-0.3122	-0.2781	-0.2831	-0.2704	-0.2707	-0.2717
0.4531	-0.1712	-0.1634	-0.1706	-0.1703	-0.1711	-0.1065	-0.1123	-0.1038	-0.1039	-0.1046
0.5000	-0.1148	-0.1081	-0.1149	-0.1147	-0.1153	-0.0608	-0.0633	-0.0602	-0.0602	-0.0606
0.6172	0.0214	0.0278	0.0190	0.0191	0.0189	0.0570	0.0643	0.0527	0.0527	0.0531
0.7344	0.1626	0.1689	0.1560	0.1561	0.1563	0.1872	0.2013	0.1779	0.1782	0.1792
0.8516	0.2909	0.2932	0.2794	0.2795	0.2799	0.3330	0.3444	0.3173	0.3179	0.3192
0.9531	0.5589	0.5615	0.5539	0.5541	0.5546	0.4660	0.4691	0.4523	0.4528	0.4537
0.9609	0.6176	0.6196	0.6134	0.6135	0.6140	0.5112	0.5145	0.4996	0.5001	0.5009
0.9688	0.6844	0.6856	0.6809	0.6810	0.6814	0.5749	0.5779	0.5656	0.5660	0.5667
0.9766	0.7584	0.7586	0.7554	0.7555	0.7558	0.6593	0.6613	0.6521	0.6524	0.6530

model, Guos model and the He-Luo model) and the reference results are observed especially in the regions of high shear stress (i.e. $0<y<0.2$, $0.8<y<1$ in the vertical centerline and $0<x<0.2$, $0.8<x<1$ in the horizontal centerline), and these errors become severer with increasing Re. On the contrary, the results from the present model accord well with those of U. Ghia [32] in these areas.

To quantify the comparisons of the four LB models, the magnitudes of the velocity components on the centerline with are listed in Tables 1 and 2. We pick four typical points ($y=0.0547$, 0.0625, 0.0703, 0.1016) in the vertical centerline near the bottom wall. At Re=400, the relative errors of other three LB model exceed 9%, whereas those of the present model are about 5%. As the Reynolds number increases to 1000, the relative errors of three conventional models are over 10%, while those of the present model are about 1%. Similarly, four typical points ($x=0.0625$, 0.0703, 0.0781, 0.0938) in the horizontal central line near the left wall are adopted. The relative errors for the other three models exceed 6%, and for the present model are less than 1%, for both Re=400 and 1000.

4.1.2 The mass conservation

In the Guo's model and the present model, the basic assumption that the fluid density of the incompressible flow is a constant is introduced, the macroscopic fluid density, i.e. $\sum_\alpha f_\alpha$, is assumed to be 0 and 1 in the Guo's model and the present model, respectively. However, in the practical simulations with these two models, the mass conservation is not preserved exactly, and the nonzero mass differences can be regarded as a kind of

https://doi.org/10.4208/cicp.091014.030515a Published online by Cambridge University Press

Table 2: The comparisons of y-velocity on the horizontal centerline for Re=400 and 1000.

	Re=400					Re=1000				
X	U. Ghia	Present Model	Guo's Model	He-Luo Model	Standard Model	U. Ghia	Present Model	Guo's Model	He-Luo Model	Standard Model
0.0625	0.1836	0.1816	0.1706	0.1710	0.1706	0.2749	0.2734	0.2552	0.2558	0.2563
0.0703	0.1971	0.1954	0.1835	0.1839	0.1835	0.2901	0.2890	0.2699	0.2706	0.2711
0.0781	0.2092	0.2076	0.1951	0.1954	0.1951	0.3035	0.3027	0.2828	0.2835	0.2841
0.0938	0.2297	0.2284	0.2147	0.2151	0.2147	0.3263	0.3256	0.3047	0.3054	0.3060
0.1563	0.2812	0.2801	0.2646	0.2650	0.2646	0.3710	0.3698	0.3500	0.3506	0.3514
0.2266	0.3020	0.2990	0.2863	0.2866	0.2864	0.3308	0.3312	0.3168	0.3171	0.3181
0.2344	0.3017	0.2984	0.2864	0.2866	0.2865	0.3224	0.3232	0.3091	0.3094	0.3103
0.5000	0.0519	0.0480	0.0542	0.0541	0.0542	0.0253	0.0246	0.0257	0.0256	0.0257
0.8047	-0.3860	-0.3803	-0.3724	-0.3724	-0.3726	-0.3197	-0.3250	-0.3027	-0.3032	-0.3044
0.8594	-0.4499	-0.4477	-0.4315	-0.4316	-0.4310	-0.4267	-0.4224	-0.4102	-0.4106	-0.4114
0.9063	-0.2383	-0.3862	-0.3646	-0.3648	-0.3636	-0.5155	-0.5124	-0.4937	-0.4941	-0.4946
0.9453	-0.2285	-0.2341	-0.2177	-0.2179	-0.2168	-0.3919	-0.3926	-0.3674	-0.3679	-0.3682
0.9531	-0.1925	-0.1981	-0.1837	-0.1838	-0.1829	-0.3371	-0.3391	-0.3157	-0.3162	-0.3165
0.9609	-0.1566	-0.1619	-0.1497	-0.1498	-0.1491	-0.2767	-0.2800	-0.2594	-0.2598	-0.2600
0.9688	-0.1215	-0.1263	-0.1165	-0.1165	-0.1159	-0.2139	-0.2183	-0.2013	-0.2016	-0.2018

Table 3: The mass differences pertaining to the present model and the Guo's model.

	129×129			257×257		
	Re=100	Re=400	Re=1000	Re=100	Re=400	Re=1000
Guo's model	1.74E-08	9.52E-08	1.35E-07	9.29E-09	2.08E-08	2.89E-08
Present model	7.45E-08	3.66E-07	5.81E-07	4.15E-08	6.35E-08	1.18E-07

density fluctuations. A mean density is defined as

$$\bar{\rho}=\frac{\sum_{i,j}|M_0(i,j)|}{N_xN_y}, \tag{4.3}$$

and the mass differences $\bar{\rho}$ and $\bar{\rho}-1$ respectively for the Guo's model and the present model are given in Table 3, additionally, the distribution of the density fluctuations pertaining to the present model is shown in Fig. 2. Obviously, the effects of such density fluctuations are quite negligible since the mass differences in Table 3 are less than 6e-7 and can be damped by a finer lattice. Moreover, these density fluctuations are concentrated near the singularities of the cavity, as demonstrated in Fig. 2.

https://doi.org/10.4208/cicp.091014.030515a Published online by Cambridge University Press



Figure 2: The distribution of the density fluctuations pertaining to the present model for the case of Re$=1000$ with grid 257×257.

4.1.3 The cavity flow with high Re

To evaluate the stability features of the present model, the simulations of the cavity flow with high Re (Re$=3200$, 5000, 7500, 10000) are performed with the 257×257, 385×385, and 513×513 grid for the last two cases, respectively and basic flow structures are plotted in Fig. 3. We note that, the 2D driven cavity flow is extracted from the corresponding 3D

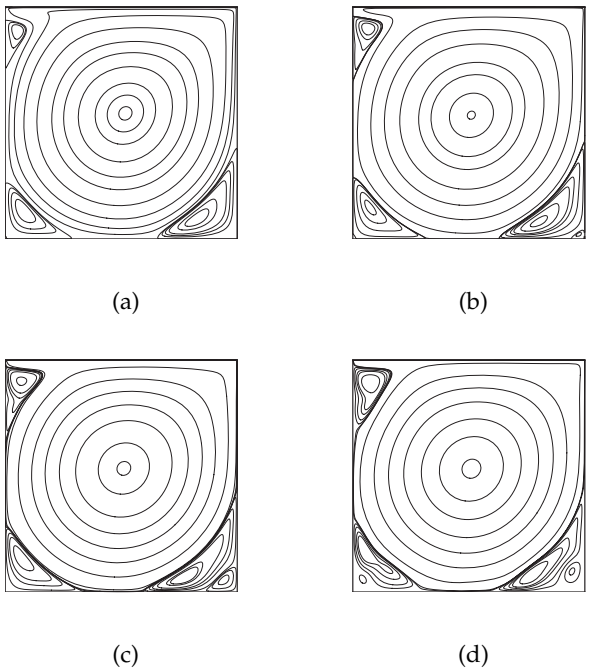


Figure 3: The streamlines for the cavity flow with Re$=3200$ (a), Re$=5000$ (b), Re$=7500$ (c) and Re$=10000$ (d). Note: the solutions for the case of Re$=10000$ are unstable, and Fig. 4(d) indicates the flow structures at some certain time.

https://doi.org/10.4208/cicp.091014.030515a Published online by Cambridge University Press

Table 4: The locations of the primary and secondary vortices.

		Primary		Secondary (Left)		Secondary (Right)	
		x	y	x	y	x	y
Re=3200	U. Ghia	0.5165	0.5469	0.0859	0.1094	0.8125	0.0859
	Present	0.5170	0.5410	0.0813	0.1195	0.8244	0.0850
Re=5000	U. Ghia	0.5117	0.5352	0.0703	0.1367	0.8086	0.0742
	Present	0.5099	0.5331	0.0738	0.1354	0.8010	0.0729
Re=7500	U. Ghia	0.5117	0.5322	0.0645	0.1504	0.7813	0.0625
	Present	0.5107	0.5324	0.0683	0.1477	0.7741	0.0633
Re=10000	U. Ghia	0.5117	0.5333	–	–	–	–
	Present	0.5052	0.5277	–	–	–	–

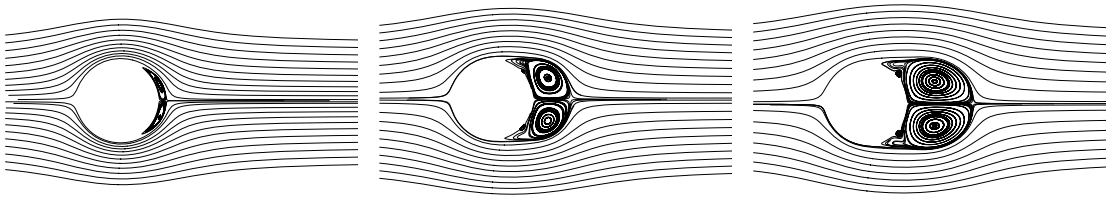
infinitely long cavity flow. Detailed stability analyses in the literature [35–38] indicates that, the infinitely long cavity flow is prone to instability (from 2D steady flow to 3D steady flow) with critical Re, $\mathrm{Re}_c = 780$. Moreover, stability investigations in previous work [39–41] also demonstrate that the critical Re for the instability from 2D steady flow to 2D oscillating flow in cavity flow is $8000 \leq \mathrm{Re}_c \leq 8050$. In [42], the critical Re_c is about $\mathrm{Re}_c = 8018$. Therefore, although some previous work [32, 44] reports stable solutions for Re= 10000, the solutions at this Re are not stable any more and the instability (Hopf bifurcation) occurs at around Re=8000 [39–43, 45]. With the present model, accurate and stable solutions for Re= 3200, 5000, 7500 are obtained, as demonstrated in Table 4 and Fig. 3. For the case of Re= 10000, the locations and configurations for the secondary vortices are unstable and vary with time, which accords with the reference results [39].

4.2 The unsteady flow past an impulsively started cylinder

The time-dependent flow past an impulsively started cylinder is a classical benchmark test for unsteady flow. This problem is especially challenging and interesting because, in the early stage, the flow reveals many complex phenomena. In particular, as suggested by Li et al. in [46], the simulation results of the drag history (more specifically, the pressure drag) for short time immediately after the impulsive start may provide some insights to the compressibility effect of the LB model. There have been a plethora of results from simulations by using various numerical methods such as finite difference schemes [47, 48], vortex methods [49] and also the LB methods [46, 50, 51]. In this work, all the concerned LB models are applied to the unsteady benchmark test to compare their performances.

The flow is confined in a rectangular domain where the upper and lower boundaries are periodic, a uniform velocity profile $U = c_s Ma$ is imposed at the inlet, and the outflow is a constant pressure boundary. The Re depends on the velocity U at the inlet and the cylinder diameter D as $\mathrm{Re} = UD/\nu$. The dimensionless time is defined by $T = 2tU/D$.

https://doi.org/10.4208/cicp.091014.030515a Published online by Cambridge University Press



(a) (b) (c)

Figure 4: Streamlines for flow past the cylinder with Re=550 at $T=1$ (a), 3 (b) and 5 (c).

The velocity field is initialized with the potential flow solution:

$$u_r = U\left(1-\frac{D^2}{4r^2}\right)\cos\theta, \quad u_\theta = -U\left(1+\frac{D^2}{4r^2}\right)\sin\theta, \tag{4.4}$$

and the velocity components in Cartesian coordinates read

$$u_x = u_r\cos\theta - u_\theta\sin\theta, \quad u_y = u_r\sin\theta + u_\theta\cos\theta. \tag{4.5}$$

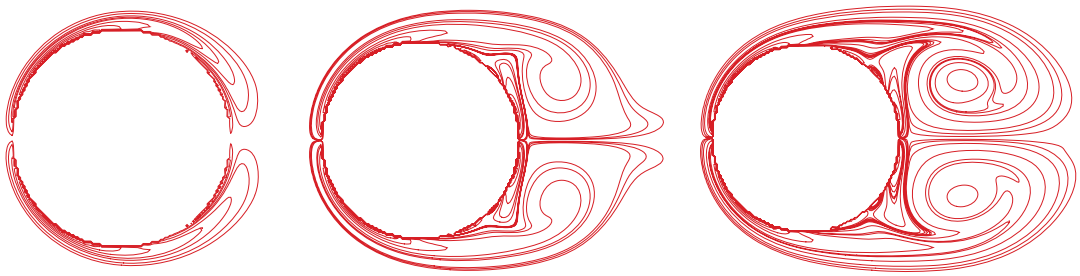
In accordance with above initial velocity field, the distribution functions are initialized following the procedure detailed in [28,50,52]. As for the boundary treatment for the circular cylinder, the curved boundary scheme proposed by Yu et al. [53], which provides a unified expression for the unknown distribution functions at the boundary nodes for various geometric parameters (i.e. the fraction of the intersected lattice links), is applied. In addition, the momentum exchange method [54] is introduced to evaluate the interaction force F between the solid cylinder and the surrounding fluid after each collision step. The drag coefficient is then calculated as

$$C_D = F_x/(\rho U^2 r). \tag{4.6}$$

For Re=40, the cylinder with $D=40$ is centered within a $100D\times 100D$ domain. For the case of Re=550, $D=100$, and the cylinder is located at $(20D, 17D)$ in the domain $60D\times 34D$. The Mach number is 0.173 for both cases. The streamlines and the vorticity contours for Re=550 at $T=1,2,3$ are plotted in Figs. 4 and 5. The complex flow phenomena such as the development of the secondary vortices as well as their impact on the evolution of the primary vortices are successfully captured by the present model and such unsteady features are in good agreement with the results in the literature [46,49].

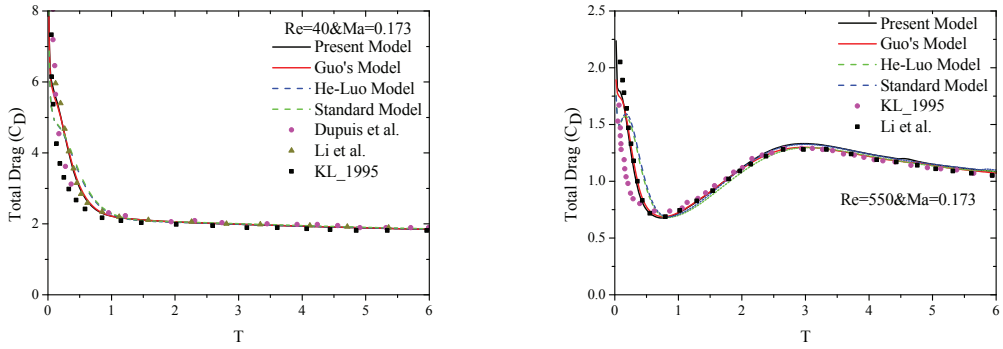
For impulsively started flow, another representative unsteady feature is the steep change of the drag coefficient at the onset of the impulsive start. Comparisons of the total drag history for Re=40 and 550 are given in Fig. 6, which indicates that the total drag resulted from all the LB models accord well with the reference results at $T\geq 1$. Particularly, the flow at Re=40 reaches a steady state after a sufficiently long time ($T\geq 25$), and the relevant drag coefficient C_D and wakelength L/D, obtained from the present

https://doi.org/10.4208/cicp.091014.030515a Published online by Cambridge University Press



(a) (b) (c)

Figure 5: Contours of vorticity in the vicinity of the cylinder with Re=550 at $T=1$ (a), 3 (b) and 5 (c).

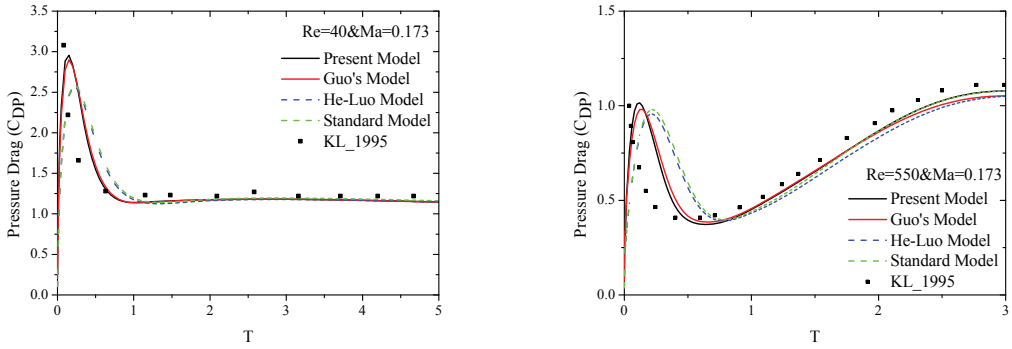


(a) (b)

Figure 6: Time evolution of the total drag with Re= 40 (a) and 550 (b), the reference results from the literature [46, 49, 50] are notated as 'Li et al.', 'KL_1995' and 'Dupuis et al.', respectively.

model, are 1.59 and 2.15, respectively. These results accord well with those in the literature: for the wakelength, $L/D=2.245$ in Ref. [55] and 2.17 in Ref. [46]; for the drag coefficient, $C_D=1.60$ in Ref. [56] and 1.55 in Ref. [46]. However, for $T<1$, the visible discrepancies are found between the two sets of LB models: the results from Guo's model and the present model are more in line with those in the literature [46, 49] than other two LB models. It is reasonable to attribute such discrepancies of the standard model and the He-Luo model to the compressibility error, since the time derivative term of the pressure in the continuity equation, which is eliminated by Guo's model and the present model, may affect the time-dependent simulations. Therefore, the Guo's model and the present model have the advantage that the unsteady compressibility error is removed and the incompressibility is supposedly satisfied. According to the elliptic incompressibility condition, weak perturbations propagate at infinite speed of sound in incompressible flows. However, like all conventional LB algorithms, the Guo's model and the present model are essentially an explicit finite difference approximation of the macroscopic equations [7, 8].

https://doi.org/10.4208/cicp.091014.030515a Published online by Cambridge University Press



(a) (b)

Figure 7: Time evolution of the pressure drag component with Re=40 (a) and 550 (b), all the results from the LB simulations are compared with the reference results [49] notated as 'KL_1995'.

Therefore, a finite sound speed is restricted by the CFL stability criterion. In this regard, the Guo's model and the present model are still not completely incompressible.

In order to further prove the above discussion, the pressure drag component of the total drag, C_{Dp}, is successively studied

$$C_{Dp} = F_{px}/(\rho U^2 r), \tag{4.7}$$

$$F_p = \int (-pI) \bullet \mathbf{n} dS. \tag{4.8}$$

Fig. 7 demonstrates the pressure drag history obtained from the LB simulations with $Ma = 0.173$. It indicates that all the LB models provide accurate results for both cases at $T \geq 1$. However, when $T < 1$ the pressure drag history resulted from all the LB models shows quite different behavior. As discussed by Li et al. in [46], at the early stage immediately after the impulsive start, the pressure drag is expected to decrease at a speed inversely proportional to the square root of time, which is the direct result of the elliptic incompressibility condition. While in the LB simulations, a very short yet finite time (T_{peak}) is required to allow the pressure drag to reach its maximum after the impulsive start as shown in Fig. 7. After that, it decrease rapidly and converge to the reference solutions.

As mentioned above, although the incompressible N-S equations are obtained in both the Guo's model and the present model, the information in the flow travels at finite speed because of the intrinsic explicit finite difference nature in LB algorithms, which departs from the incompressibility condition. Therefore, like the standard model and the He-Luo model, the pressure drag history obtained from the Guo's model and the present model also departs slightly from the reference results [49] at $T < 1$. However, owing to the compressibility error term $\frac{1}{RT}\frac{\partial p}{\partial t}$ is eliminated in both the Guo's model and the present

https://doi.org/10.4208/cicp.091014.030515a Published online by Cambridge University Press

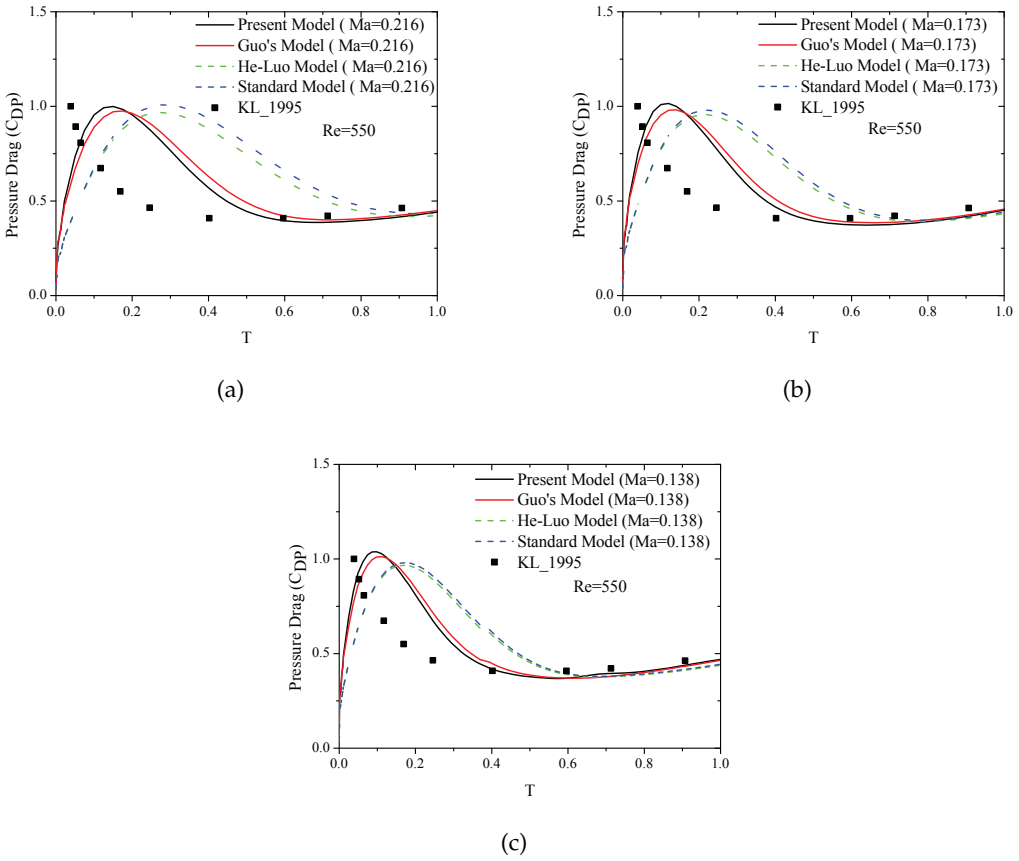


Figure 8: Comparisons of the pressure drag history for different Ma with Re$=$550, all the results from the LB simulations are compared with the reference results [49] notated as 'KL_1995'.

model, further comparisons suggest that the T_{peak} of these two models are quite less than those of the standard model and the He-Luo model as exhibited in Figs. 7 and 8.

5 Summary and conclusion

In this work, under the basic assumption that the fluid density is a uniform constant and the fluid pressure is independent of density, an alternative LB model for incompressible flow is proposed by using the moment expansions. Consistent with the Guo's model, the incompressible N-S equations is derived from the present model, and the compressibility error in the standard model and He-Luo model is theoretically removed by setting the fluid density to be a uniform constant. In addition, the stability of the present model is enhanced by introducing an additional relaxation time pertaining to the non-hydrodynamic modes.

https://doi.org/10.4208/cicp.091014.030515a Published online by Cambridge University Press

Numerical results of the steady and unsteady benchmark tests demonstrate that: the present model provides better accuracy near the solid walls for the cavity flow, and the time-dependent flow features obtained from the present model and Guo's model are more in line with the incompressibility condition in simulating flow past an impulsively started cylinder.

Acknowledgments

This work is supported by the Fundamental Research Funds for the Central Universities (No. CDJZR13248801), Program for Changjiang Scholars and Innovative Research Team in University (No. IRT13043), and Research Fund for the Doctoral Program of Higher Education of China (No. 20110191110037).

References

[1] W.A. Yong, L.-S. Luo, Accuracy of the viscous stress in the lattice Boltzmann equation with simple boundary conditions, Phys. Rev. E 86 (2012) 065701(R).
[2] A.J.C. Ladd, Numerical simulations of particulate suspensions via a discretized Boltzmann equation. Part 1 Theoretical foundation, J. Fluid Mech. 271 (1994) 285-309.
[3] P. Lallemand, L.-S. Luo, Lattice Boltzmann method for moving boundaries, J. Comput. Phys. 184 (2003) 406-421.
[4] X.W. Shan, H.D. Chen, Lattice Boltzmann model for simulating flows with multiple phases and components, Phys. Rev. E 47 (1993) 1815-1819.
[5] X.W. Shan, H.D. Chen, Simulation of nonideal gases and liquid-gas phase transitions by the Lattice Boltzmann equation, Phys. Rev. E 49 (1994) 2941-2948.
[6] T. Lee, L. Liu, Lattice Boltzmann simulations of micron-scale drop impact on dry surfaces, J. Comput. Phys. 229 (2010) 8045-8062.
[7] M. Junk, A finite difference interpretation of the lattice Boltzmann method, Numer. Meth. Part D E 17 (2001) 383-402.
[8] M. Junk, A. Klar, Discretizations for the incompressible Navier-Stokes equations based on the lattice Boltzmann method, A SIAM J. Sci. Comput. 22 (2000) 1-19.
[9] P.J. Dellar, Incompressible limits of lattice Boltzmann equations using multiple relaxation times, J. Comput. Phys. 190 (2003) 351-370.
[10] P. Lallemand, L.S. Luo, Theory of lattice Boltzmann method: dispersion, dissipation, isotropy, Galilean invariance, and stability, Phys. Rev. E 61 (2000) 6546-6562.
[11] S. Chapman, T.G. Cowling, The mathematical theory of non-uniform gases, 3rd edition, Cambridge: Cambridge University Press; 1970.
[12] P.J. Dellar, Bulk and shear viscosities in lattice Boltzmann equations, Phys. Rev. E 64 (2001) 031203.
[13] P.J. Dellar, Nonhydrodynamic modes and a priori construction of shallow water lattice Boltzmann equations, Phys. Rev. E 65 (2002) 036309.
[14] X.Y. He, L.S. Luo, Lattice Boltzmann model for the incompressible Navier-Stokes equation, J. Stat. Phys. 88 (1997) 927-944.

https://doi.org/10.4208/cicp.091014.030515a Published online by Cambridge University Press

[15] L.S. Luo, W. Liao, X.W. Chen, Y. Peng, W. Zhang, Numerics of the lattice Boltzmann method: effects of collision models on the lattice Boltzmann simulations, Phys. Rev. E 83 (2011) 056710.
[16] Z.L. Guo, B.C. Shi, N.C. Wang, Lattice BGK model for the incompressible Navier-Stokes equation, J. Comput. Phys. 165 (2000) 288-306.
[17] H. Grad, On the Kinetic theory of rarefied gases, Commun. Pure Appl. Math. 2 (1949) 331-407.
[18] X.W. Shan, X.Y. He, Discretization of the velocity space in the solution of the Boltzmann equation, Phys. Rev. Lett. 80 (1998) 65-68.
[19] L.Q. Zhang, Z. Zeng, H.Q. Xie, Y.X. Zhang, Y.Y. Lu, A. Yoshikawa, H. Mizuseki, Y. Kawazoe, A comparative study of lattice Boltzmann models for incompressible flow, Computers and Mathematics with Applications 68 (2014) 1446-1466.
[20] P.J. Dellar, Non-hydrodynamic modes and general equations of state in lattice Boltzmann equations, Phys. A 362 (2006) 132-138.
[21] R. Benzi, S. Succi, M. Vergassola, Turbulence modeling by Nonhydrodynamic variables, Europhys. Lett. 13 (1990) 727-732.
[22] R. Benzi, S. Succi, M. Vergassola, The lattice Boltzmann equation: theory and applications, Phys. Rep. 222 (1992) 145-197.
[23] D. d'Humières, Generalized lattice-Boltzmann equations. In: Shizgal BD, Weave DP, editors. Rarefied Gas Dynamics: Theory and Simulations. Vol. 159 of Prog. Aatronaut. Aeronaut., 1992. p. 450-458.
[24] S. Succi, The Lattice Boltzmann Equation: For Fluid Dynamics and Beyond, Oxford University Press, Oxford, 2001.
[25] F. J. Higuera, S. Succi, R. Benzi, Lattice gas dynamics with enhanced collisions, Europhys. Lett. 9 (1989) 345-349.
[26] A. Montessori, M. La Rocca, G. Falcucci, S. Succi, Regularized lattice BGK versus highly accurate spectral methods for cavity flow simulations, Int. J. Mod. Phys. C 25 (2014) 1441003.
[27] A. Montessori, G. Falcucci, P. Prestininzi, M. La Rocca, S. Succi, Regularized lattice Bhatnagar-Gross-Krook model for two- and three-dimensional cavity flow simulations, Phys. Rev. E 89 (2014) 053317.
[28] J. Latt, B. Chopard, Lattice Boltzmann method with regularized pre-collision distribution functions, Math. Comp. Simul. 72 (2006) 165-168.
[29] P.L. Bhatnagar, E.P. Gross, M. Krook, A model for collision processes in gases. I. Small amplitude processes in charged and neutral one-component systems, Phys. Rev. 94 (1954) 511-525.
[30] Y.H. Qian, D. d'Humières, P. Lallemand, Lattice BGK models for Navier-Stokes equation, Europhys. Lett. 17 (1992) 479-484.
[31] X.Y. He, L.S. Luo, Theory of the lattice Boltzmann method: From the Boltzmann equation to the lattice Boltzmann equation, Phys. Rev. E 56 (1997) 6811-6817.
[32] U. Ghia, K.N. Ghia, C.T. Shin, High-Re solutions for incompressible flow using the Navier-Stokes equations and a multigrid method, J. Comput. Phys. 48 (1982) 387-411.
[33] S.L. Hou, Q.S. Zou, Simulation of cavity flow by the lattice Boltzmann method. J Comput Phys 118 (1995) 329-347.
[34] Z.L. Guo, C.G. Zheng, B.C. Shi, Non-equilibrium extrapolation method for velocity and pressure boundary conditions in the lattice Boltzmann method, Chin. Phys. Soc. 11 (2002) 366-374.
[35] S. Albensoeder, H.C. Kuhlmann, H.J. Rath, Three-dimensional centrifugal-flow instabilities in the lid-driven-cavity problem, Phys. Fluids 13 (2001) 121-135.

https://doi.org/10.4208/cicp.091014.030515a Published online by Cambridge University Press

[36] V. Theofilis, P.W. Duck, J. Owen, Viscous linear stability analysis of rectangular duct and cavity flows, J. Fluid Mech. 505 (2004) 249-286.
[37] J. Chicheportiche, X. Merle, X. Gloerfelt, J.C. Robinet, Direct numerical simulation and global stability analysis of three-dimensional instabilities in a lid-driven cavity, C R Mec. 336 (2008) 586-591.
[38] E. Non, R. Pierre, J.J. Gervais, Linear stability of the three-dimensional lid-driven cavity, Phys. Fluids 18 (2006) 084103.
[39] C.H. Bruneau, M. Saad, The 2D lid-driven cavity problem revisited, Comput. Fluids 35 (2006) 326-348.
[40] A. Fortin, M. Jardak, J.J. Gervais, R. Pierre, Localization of Hopf bifurcations in fluid flow problems, Int. J. Numer. Methods Fluids 24 (1997) 1185-1210.
[41] M. Sahin, R.G. Owens, A novel fully-implicit finite volume method applied to the lid-driven cavity problem, Parts I and II, Int. J. Numer. Methods Fluids 42 (2003) 1.
[42] F. Auteri, N. Parolini, L. Quartapelle, Numerical investigation on the stability of singular driven cavity flow, J. Comput. Phys. 183 (2002) 1.
[43] T.W. Pan, R. Glowinski, A projection/wave-like equation method for the numerical simulation of incompressible viscous fluid flow modeled by the Navier-Stokes equations, Comp. Fluid Dyn. 9 (2000) 2.
[44] R. Schreiber, H.B. Keller, Driven cavity flows by efficient numerical techniques, J. Comput. Phys. 49 (1983) 310-333.
[45] V.B.L. Boppana, J.S.B. Gajjar, Global flow instability in a lid-driven cavity, Int. J. Numer. Methods Fluids 62 (2010) 827-853.
[46] Y.B. Li, R. Shock, R.Y. Zhang, H.D. Chen, Numerical study of flow past an impulsively started cylinder by the lattice-Boltzmann method, J. Fluid Mech. 519 (2004) 273-300.
[47] C. Aderson, M. Reider, A high order explicit method for the computations of flow about a circular cylinder, J. Comput. Phys. 125 (1996) 207-224.
[48] W. Collins, S. Dennis, Flow past an impulsively started circular cylinder, J. Fluid Mech. 60 (1973) 105-127.
[49] P. Koumoutsakos, A. Leonard, High-resolution simulations of the flow around an impulsively started cylinder using vortex methods, J. Fluid Mech. 296 (1995) 1-38.
[50] A. Dupuis, P. Chatelain, P. Koumoutsakos, An immersed boundary-lattice-Boltzmann method for simulation of flow past an impulsively started cylinder, J. Comput. Phys. 227 (2008) 4486-4498.
[51] J.C.G. Verschaeve, B. Müller, A curved no-slip boundary condition for the lattice Boltzmann method, J. Comput. Phys. 229 (2010) 6781-6803.
[52] B. Chopard, M. Droz, Cellular automata modeling of physical systems, Cambridge University Press, 1998.
[53] D.Z. Yu, R.W. Mei, W. Shyy, A unified boundary treatment in lattice Boltzmann method, 41st Aerospace Science Meeting and Exhibit, 6-9 January 2003.
[54] A.J.C. Ladd, Numerical simulation of particular suspensions via a discretized Boltzmann equation, Part 2, Numerical results, J. Fluid Mech. 271 (1994), 311-339.
[55] X.Y. He, G. Doolen, Lattice Boltzmann method on curvilinear coordinates system: Flow around a circular cylinder, J. Comput. Phys. 134 (1997) 306.
[56] A.A. Delouei, M. Nazari, M.H. Kayhani, S. Succi, Non-Newtonian unconned ow and heat transfer over a heated cylinder using the direct-forcing immersed boundarythermal lattice Boltzmann method, Phys. Rev. E 89 (2014) 053312.

https://doi.org/10.4208/cicp.091014.030515a Published online by Cambridge University Press